

Formation of Local Resonance Band Gaps in Finite Acoustic Metamaterials: A Closed-form Transfer Function Model

H. Al Ba'ba'a^a, M. Nouh^{a,*}, T. Singh^a

^a*Dept. of Mechanical & Aerospace Engineering, University at Buffalo (SUNY), Buffalo, NY*

Abstract

The objective of this paper is to use transfer functions to comprehend the formation of band gaps in locally resonant acoustic metamaterials. Identifying a recursive approach for any number of serially arranged locally resonant mass in mass cells, a closed form expression for the transfer function is derived. Analysis of the end-to-end transfer function helps identify the fundamental mechanism for the band gap formation in a finite metamaterial. This mechanism includes (a) repeated complex conjugate zeros located at the natural frequency of the individual local resonators, (b) the presence of two poles which flank the band gap, and (c) the absence of poles in the band-gap. Analysis of the finite cell dynamics are compared to the Bloch-wave analysis of infinitely long metamaterials to confirm the theoretical limits of the band gap estimated by the transfer function modeling. The analysis also explains how the band gap evolves as the number of cells in the metamaterial chain increases and highlights how the response varies depending on the chosen sensing location along the length of the metamaterial. The proposed transfer function approach to compute and evaluate band gaps in locally resonant structures provides a framework for the exploitation of control techniques to modify and tune band gaps in finite metamaterial realizations.

Keywords: acoustic metamaterials, band gaps, transfer functions

1. Introduction

Acoustic metamaterials (AMMs) are sub-wavelength structures that consist of chains of self-repeating unit cells which house internal elastic resonators. The hallmark feature of AMMs is their ability to realize band gaps, i.e. regions of blocked wave propagation, in low frequency regimes. Band gaps in AMMs primarily depend on the resonator properties and are, thus, size-independent and mechanically tunable [1]. Unique wave propagation behavior in AMMs

*Corresponding author

Email address: mnouh@buffalo.edu (M. Nouh)

have rendered them appealing for a wide range of damping and noise control applications. Over the past few decades, AMMs have been investigated in the context of discrete lumped mass systems [2, 3], elastic bars [4, 5], flexural beams [6–14], as well as 2D membranes and plates [15–18]. Given the dependence of the band structure of the AMM unit cell on resonator parameters, multiple efforts have also been placed on piezoelectric, or actively controlled, metamaterials [19–23].

Acoustic metamaterials are most commonly modeled using a Bloch-wave propagation model of the self-repeating unit cell with periodic boundary conditions [24–28]. Wave propagation methods assume traveling wave propagation in an infinitely-long metamaterial comprised of the individual unit cells. The occurrence of band gaps in these infinite structures has been explained in light of gaps in the unit cell’s dispersion curve (band diagram) and/or the negative effective mass density concept [29, 30]. Discrepancies in the response of actual metamaterials motivated several efforts to understand band gap realizations in finite structures and the effect of imposed boundary conditions [31–33]. Significant among those is the investigation of the relationship between the borders of Bragg-effect band gaps in phononic (periodic) structures and the corresponding eigenfrequencies, explained using the phase-closure principle [32, 33]. Modal analysis has also been utilized to develop a mathematical formulation to estimate locally resonant band gaps and provide design guidelines and insights into the choice of resonators and their optimal locations [34]. To this date, however, a mathematical framework that explains and quantifies the evolution of local resonance band gaps in finite AMMs remains lacking.

In this effort, we focus on AMMs where the number of cells, as well excitation and response locations, are specified. We derive a generalized dynamic model to evaluate the input-to-output transfer function associated with such locally resonant structures, and explain the formation mechanism of the band gap in light of their frequency response and pole-zero (PZ) distributions. To facilitate the discussion and advance a closed-form solution, the analysis is carried out on a one-dimensional mass-in-mass type metamaterial. The AMM consists of a chain of spring-mass unit cells shown in Figure 1. In the presented analysis, damping elements are excluded from both the base and the local structure for two important reasons: (1) to neutralize the effect of dissipation on the band gaps, an effect that has been recently investigated in a number of efforts [35–38], and (2) to ensure that any damping captured in the numerically computed poles or zeros in the lengthy expressions of the developed dynamic model of the finite AMM are merely a result of minor errors or computational precision, as will be highlighted later in the discussion. The limiting case of the presented approach as the length of the AMM chain approaches infinity matches the traditional Bloch-wave analysis and bridges the gap between the two approaches.

Finally, the discussion is extended to explain and differentiate between the effects of sensing location (i.e., location where displacement is measured) and the effect of the number of cells on the bandwidth and degree of attenuation obtained from the local resonators. Analysis of AMMs from a dynamic systems perspective provides a physical insight into the formation of these band gaps

over a specific range of frequencies, and provides a clear distinction between the operation concepts of AMMs and tuned dynamic absorbers from a vibrations standpoint. Furthermore, explaining the behavior in terms of frequency domain tools and PZ maps sets a future framework for implementing control techniques. Finally, the investigation of finite metamaterial structures is naturally of interest since the results directly impact the fabrication of realistic and physically realizable, rather than purely theoretical, AMMs.

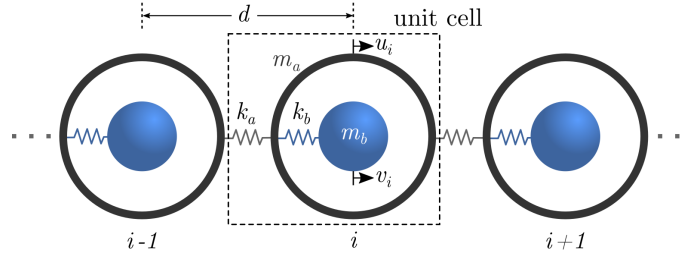


Figure 1: A lumped mass-in-mass locally resonant acoustic metamaterial

2. Dynamics of 1-D Acoustic Metamaterials

2.1. Wave Dispersion Analysis

The simplest example of an AMM is a periodic series of spring-mass systems hosting internal spring-mass resonators, as shown in Figure 1. For an AMM with cell spacing d , identical outer masses m_a and inner masses m_b connected via springs k_a and k_b , the governing motion equations for the i^{th} unit can be derived as:

$$\begin{bmatrix} m_a & 0 \\ 0 & m_b \end{bmatrix} \begin{Bmatrix} \ddot{u}_i \\ \ddot{v}_i \end{Bmatrix} + \begin{bmatrix} 2k_a + k_b & -k_b \\ -k_b & k_b \end{bmatrix} \begin{Bmatrix} u_i \\ v_i \end{Bmatrix} + \begin{bmatrix} -k_a & -k_a \\ 0 & 0 \end{bmatrix} \begin{Bmatrix} u_{i-1} \\ u_{i+1} \end{Bmatrix} = \begin{Bmatrix} 0 \\ 0 \end{Bmatrix} \quad (1)$$

where u_i and v_i represent the displacements of m_a and m_b of the i^{th} cell, respectively. By applying the harmonic wave solution to the above motion equations, the dispersion relation can be derived as [3]

$$A_1 \omega^4 + A_2 \omega^2 + A_3 = 0 \quad (2)$$

with

$$A_1 = m_a m_b, \quad A_2 = -[(m_a + m_b)k_b + 2m_b k_a (1 - \cos \bar{\beta})], \quad A_3 = 2k_a k_b (1 - \cos \bar{\beta})$$

where ω is the angular frequency and $\bar{\beta}$ is the normalized wavenumber given by $2\pi d/\lambda$ where λ is the wavelength, or the spatial period of the propagating wave.

Equation (2) can be normalized in terms of the mass ratio $m_r = m_b/m_a$, the stiffness ratio $k_r = k_b/k_a$, and a non-dimensional frequency $\Omega = \omega/\omega_b$ to give

$$\Omega^4 - [(1 + m_r) + 2\Gamma(1 - \cos \bar{\beta})]\Omega^2 + 2\Gamma(1 - \cos \bar{\beta}) = 0 \quad (3)$$

where $\omega_b = \sqrt{k_b/m_b}$ is the natural frequency of the local resonator and $\Gamma = \frac{m_r}{k_r}$. Eq. (3) can be used to compute the dispersion curves (band structure) $\Omega(\bar{\beta})$ of the AMM. Figure 2(a) shows these curves for an AMM with $m_a = 1$ kg, $m_b = 0.3m_a$, $k_a = 4.8$ GN/m and $k_b = 0.1k_a$. The shaded region represents the frequency range of the local resonance band gap which also spans the negative effective mass m_e region of an equivalent homogeneous material, as shown in Figure 2(b), and given by [29]

$$m_e = m_a + \frac{m_b\omega_b^2}{\omega_b^2 - \omega^2}. \quad (4)$$

The band gap splits the dispersion curve of the metamaterial into acoustic and optic branches (where $\bar{\beta}$ is purely real) representing in-phase and out-of-phase propagating wave modes in the outer mass and the internal resonator. The theoretical bounds of the band gap can be obtained directly from Eq. (3). By setting $\bar{\beta} = \pi$, the solution of the dispersion relation yields the lower bound Ω_l which is, for this case, equal to 0.9867. Generally, Ω_l will vary with both the stiffness and the mass ratios of the individual cell and is given by

$$\Omega_l = \frac{1}{\sqrt{2}} \sqrt{(1 + m_r + 4\Gamma) - \sqrt{(1 + m_r + 4\Gamma)^2 - 16\Gamma}} \quad (5)$$

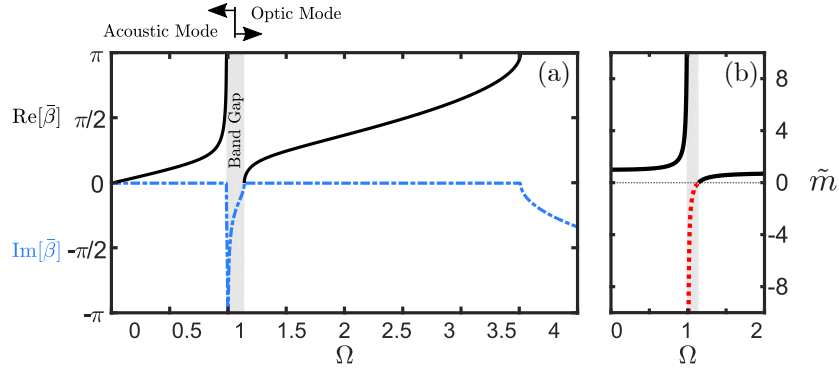


Figure 2: (a) Band structure of the AMM unit cell obtained from its dispersion relations and (b) the corresponding normalized effective mass $\tilde{m} = \frac{m_e}{(m_a + m_b)}$. The shaded region highlights the band gap frequency span in (a) which matches the negative effective mass region in (b)

On the other hand, the upper bound of the band gap Ω_u can be obtained by setting $\bar{\beta} = 0$ to obtain a non-zero solution of

$$\Omega_u = \sqrt{1 + m_r} \quad (6)$$

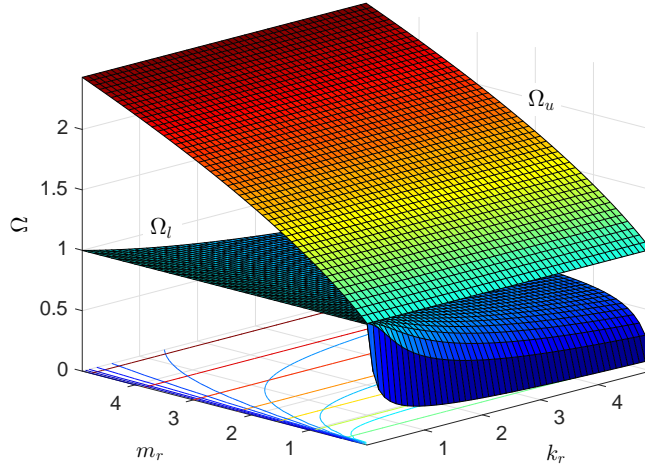


Figure 3: Variation of the local resonance band gap bounds, Ω_l and Ω_u , with m_r and k_r .

which, unlike the lower bound, solely depends on the mass ratio m_r .

Figure 3 graphically depicts the effect of both the mass and stiffness ratios on the local resonance band gap bounds, which will be relevant to the discussion in Sec. 4. Important to note here is that the AMM band gap does not necessarily start at the natural frequency of the local resonator (i.e. at $\Omega_l = 1$), which is a common misconception. It can be also seen that as k_r approaches zero, the solution of Ω_l in Eq. (5) approaches 1. However, a larger k_r shifts the lower end of the band gap down, effectively shortening the acoustic mode. In which case, the AMM band gap (and attenuation of incident waves) can start at a frequency lower than the local resonance. Although existent, the effect of m_r on Ω_l is however minimal for m_r values larger than 1. On the other hand, the upper bound of the band gap Ω_u is solely influenced by m_r which also shapes the final structure of the optic branch. Finally, it is worth noting that an exact $\Omega_l = 1$ value is not achievable from Eq. (5) for any combination of m_r and k_r . However, $\Omega_l = 0$ may be obtained as a result of a zero Γ and a non-zero m_r , (i.e. an infinitely stiff local spring), which is a purely theoretical case.

2.2. Structural dynamics of a finite AMM

Since the AMM in Figure 1 is described by a series of discrete mechanical elements, the profile of the propagating waves is captured by the discretized displacement field given by the vectors \mathbf{u} and \mathbf{v} along the length L of the AMM, where

$$\mathbf{u} = \{u_1 \quad u_2 \quad \dots \quad u_i \quad \dots \quad u_n\}^T \quad (7)$$

and

$$\mathbf{v} = \{v_1 \quad v_2 \quad \dots \quad v_i \quad \dots \quad v_n\}^T \quad (8)$$

For an AMM of n cells, the equations of motion of the end cells slightly differ from the middle ones. For any i^{th} cell where $2 \leq i \leq n-1$, the motion is given by

$$\begin{aligned} m_a \ddot{u}_i + (2k_a + k_b)u_i - k_a u_{i-1} - k_a u_{i+1} - k_b v_i &= 0 \\ m_b \ddot{v}_i + k_b v_i - k_b u_i &= 0 \end{aligned} \quad (9)$$

while the first ($i = 1$) and last ($i = n$) cells are described by

$$\begin{aligned} m_a \ddot{u}_1 + (k_a + k_b)u_1 - k_a u_2 - k_b v_1 &= F \\ m_b \ddot{v}_1 + k_b v_1 - k_b u_1 &= 0 \end{aligned} \quad (10)$$

and

$$\begin{aligned} m_a \ddot{u}_n + (k_a + k_b)u_n - k_a u_{n-1} - k_b v_n &= 0 \\ m_b \ddot{v}_n + k_b v_n - k_b u_n &= 0 \end{aligned} \quad (11)$$

where F represents the forcing acting on the outer mass of the first unit cell. As a result, the steady-state oscillations of a finite AMM subject to the external sinusoidal excitation \mathbf{F} is given by

$$\begin{Bmatrix} \mathbf{u} \\ \mathbf{v} \end{Bmatrix} = \left(-\omega^2 \begin{bmatrix} \mathbf{M}_u & \mathbf{0} \\ \mathbf{0} & \mathbf{M}_v \end{bmatrix} + \begin{bmatrix} \mathbf{K}_u & -\mathbf{K}_v \\ -\mathbf{K}_v & \mathbf{K}_v \end{bmatrix} \right)^{-1} \begin{Bmatrix} \mathbf{F} \\ \mathbf{0} \end{Bmatrix} \quad (12)$$

where the sub-components of the mass and stiffness matrices can be obtained from

$$\mathbf{M}_u = \begin{bmatrix} m_a & & & \\ & m_a & & \\ & & \ddots & \\ & & & m_a \end{bmatrix} \quad \mathbf{M}_v = \begin{bmatrix} m_b & & & \\ & m_b & & \\ & & \ddots & \\ & & & m_b \end{bmatrix} \quad (13)$$

$$\mathbf{K}_v = \begin{bmatrix} k_b & & & \\ & k_b & & \\ & & \ddots & \\ & & & k_b \end{bmatrix} \quad (14)$$

$$\mathbf{K}_u = \begin{bmatrix} k_a + k_b & -k_a & & & \\ -k_a & 2k_a + k_b & -k_a & & \\ & & \ddots & \ddots & \\ & & & -k_a & 2k_a + k_b & -k_a \\ & & & & -k_a & k_a + k_b \end{bmatrix} \quad (15)$$

while \mathbf{F} is equal to

$$\mathbf{F} = \{F \ 0 \ \dots \ 0\}^T \quad (16)$$

2.3. Analytical formula for the AMM's natural frequencies

The free vibration of an n -cell AMM is given by

$$\begin{bmatrix} \mathbf{M}_u & \mathbf{0} \\ \mathbf{0} & \mathbf{M}_v \end{bmatrix} \begin{Bmatrix} \ddot{\mathbf{u}} \\ \ddot{\mathbf{v}} \end{Bmatrix} + \begin{bmatrix} \mathbf{K}_u & -\mathbf{K}_v \\ -\mathbf{K}_v & \mathbf{K}_v \end{bmatrix} \begin{Bmatrix} \mathbf{u} \\ \mathbf{v} \end{Bmatrix} = \begin{Bmatrix} \mathbf{0} \\ \mathbf{0} \end{Bmatrix} \quad (17)$$

Assuming harmonic motion, and normalizing the excitation frequency with ω_b , we obtain

$$\begin{bmatrix} \mathbf{\Omega} - \mathbf{\Gamma\Psi} - m_r \mathbf{I} & m_r \mathbf{I} \\ \mathbf{I} & \mathbf{\Omega} - \mathbf{I} \end{bmatrix} \begin{Bmatrix} \mathbf{u} \\ \mathbf{v} \end{Bmatrix} = \begin{Bmatrix} \mathbf{0} \\ \mathbf{0} \end{Bmatrix} \quad (18)$$

where \mathbf{I} is the identity matrix and $\mathbf{\Omega}$ and $\mathbf{\Psi}$ are given by

$$\mathbf{\Omega}_{n \times n} = \begin{bmatrix} \Omega^2 & & & & \\ & \Omega^2 & & & \\ & & & \ddots & \\ & & & & \Omega^2 \end{bmatrix} \quad (19)$$

$$\mathbf{\Psi}_{n \times n} = \begin{bmatrix} 1 & -1 & & & \\ -1 & 2 & -1 & & \\ & & \ddots & \ddots & \ddots \\ & & & -1 & 2 & -1 \\ & & & & -1 & 1 \end{bmatrix} \quad (20)$$

It is seen from Eq. (18) that $\mathbf{u} + (\mathbf{\Omega} - \mathbf{I})\mathbf{v} = \mathbf{0}$, which allows us to reduce the left-hand matrix to be in terms of \mathbf{u} only

$$[\mathbf{\Omega}^2 - (\mathbf{\Gamma\Psi} + (m_r + 1)\mathbf{I})\mathbf{\Omega} + \mathbf{\Gamma\Psi}] \{\mathbf{u}\} = \{\mathbf{0}\} \quad (21)$$

where the dimensions of the new matrix are $n \times n$. The matrix in Eq. (21) is a symmetric tridiagonal matrix with the same diagonal elements b , except for the first and last terms, which may be written in the following general form

$$\begin{bmatrix} -\eta + b & a & & & \\ a & b & a & & \\ & & \ddots & \ddots & \ddots \\ & & & a & b & a \\ & & & & a & -\xi + b \end{bmatrix} \quad (22)$$

where $a = \Gamma(\Omega^2 - 1)$ and $b = \Omega^4 - (1 + m_r + 2\Gamma)\Omega^2 + 2\Gamma$. It has been reported that for values of ξ and η equal to $-a$, which is the case here, the eigenvalues for such a matrix takes the following form [39]

$$\lambda_k = b + 2a \cos \theta_k \quad (23)$$

where $k = 1, 2, \dots, n$ and $\theta_k = \frac{k-1}{n}\pi$. Once the eigenvalues are established, the left-hand matrix in Eq. (21) can be decomposed into $\mathbf{Q}\mathbf{\Lambda}_k\mathbf{Q}^T$ since the eigenvectors of a symmetric matrix are orthogonal. $\mathbf{\Lambda}_k$ is the eigenvalue matrix and \mathbf{Q} and \mathbf{Q}^T are the corresponding left and right eigenvector matrices, respectively. The decomposed matrix facilitates the calculation of the determinant of the original matrix (Eq. (21)). Since $|\mathbf{Q}\mathbf{Q}^T| = 1$, $|\mathbf{\Lambda}_k|$ has to be zero and the natural frequencies of an n -cell AMM are found as

$$\Omega_k^4 - (1 + m_r + 2\Gamma(1 - \cos \theta_k))\Omega_k^2 + 2\Gamma(1 - \cos \theta_k) = 0 \quad (24)$$

Each value of k gives two real positive solutions for Ω_k^2 , resulting in $2n$ values of the natural frequencies. For convenience, we define a new index q to denote the $2n$ values of natural frequencies Ω_q , where $q = 1, 2, \dots, 2n$ and $\Omega_1 < \Omega_2 < \dots < \Omega_{2n}$. Each k gives two natural frequencies at $q = k$ and $q = k + n$, resulting in Ω_k and Ω_{k+n} , which correspond to the acoustic and optic modes respectively. The eigenvectors $\mathbf{u}^{(q)}$ are given by [39]

$$u_i^{(q)} = u_i^{(k)} = u_i^{(k+n)} = \rho^{i-1} \quad (25)$$

for $k = 1$, and

$$u_i^{(q)} = u_i^{(k)} = u_i^{(k+n)} = \rho^{i-1} \cos \frac{(2k-1)(2i-1)\pi}{2n} \quad (26)$$

for $k = 2, 3, \dots, n$, and $\rho = 1$. Next, the eigenvectors of the local resonators $\mathbf{v}^{(q)}$ can be found as

$$\mathbf{v}^{(q)} = (\mathbf{I} - \mathbf{\Omega}_q)^{-1} \mathbf{u}^{(q)} \quad (27)$$

and as a result the complete eigenvector of the AMM $\mathbf{Q}^{(q)}$ is given by

$$\mathbf{Q}^{(q)} = \{\mathbf{u}^{(q)} \mathbf{v}^{(q)}\}^T \quad (28)$$

Several observations can be made from the above set of equations. First, the eigenvectors (oscillation modes) of the outer and local masses, $\mathbf{u}^{(q)}$ and $\mathbf{v}^{(q)}$, are related by the scalar $(\mathbf{I} - \mathbf{\Omega}_q)^{-1}$ which depends on the eigenfrequency Ω_q . It is evident that for $\Omega_q < 1$, $(1 - \Omega_q)$ becomes positive and consequently the outer and inner oscillate in-phase (confirming the commonly known acoustic mode in Figure 2). The opposite happens for $\Omega_q > 1$ leading to out-of-phase motion, or the optic mode. Second, Eqs. (25) and (26) reveal that the two eigenfrequencies Ω_k and Ω_{k+n} have the same outer mass eigenvector (i.e. $\mathbf{u}^{(k)} = \mathbf{u}^{(k+n)}$). Nonetheless, the complete eigenvectors $\mathbf{Q}^{(q)}$ are still unique since $\mathbf{v}^{(q)}$ is different for each value of Ω_q as depicted in Eq. (27).

Figure 4 shows the eigenvectors for $k = 4$ of an AMM with 20 cells (i.e. $q = 4$ and $q = 24$). As predicted, $u^{(4)}$ and $v^{(4)}$ oscillate in-phase, while $u^{(24)}$ and $v^{(24)}$ are out-of-phase with $u^{(24)}$ being identical to $u^{(4)}$. Finally, it is worth noting that when $k = 1$ (which corresponds to the two natural frequencies $\Omega_1 = 0$ and $\Omega_{1+n} = \sqrt{1 + m_r}$), Eq. (25) yields identical eigenvectors of ones for $\mathbf{u}^{(1)}$ and $\mathbf{u}^{(1+n)}$. In the $\Omega_1 = 0$ case, this understandably represents a rigid body mode for the unconstrained AMM. For $\Omega_{1+n} = \sqrt{1 + m_r}$, however, all the outer masses m_a of the AMM oscillate as a single body. In other words, the relative motion between the masses is absent and the connecting springs k_a do not deform. Interestingly, the same happens in the inner masses or the local resonators of the AMM. In this scenario, the motions $\mathbf{u}^{(1+n)}$ and $\mathbf{v}^{(1+n)}$ are out-of-phase such that $\mathbf{v}^{(1+n)} = \frac{-1}{m_r}\mathbf{u}^{(1+n)}$.

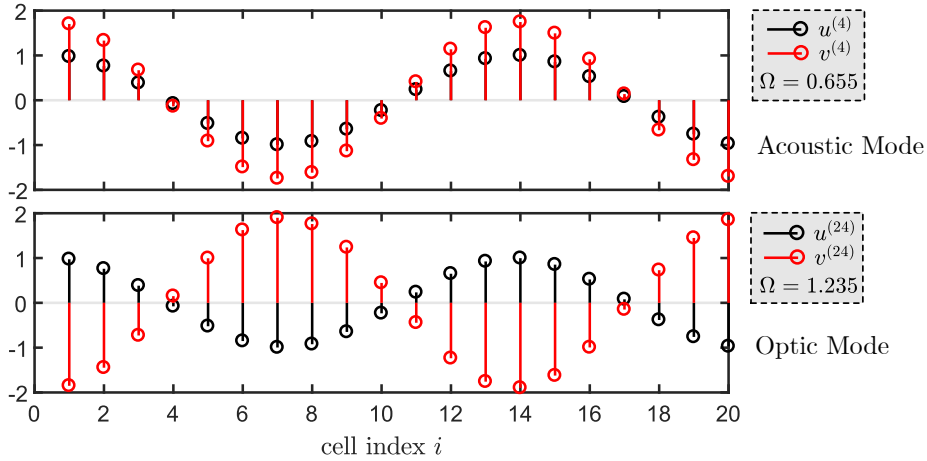


Figure 4: Mode shapes of a 20-cell AMM for $k = 4$

While this section derived an analytical solution for the eigenvalues and corresponding eigenvectors for a finite acoustic metamaterial, the following section presents a transfer function formulation to represent the input-output characteristics of a finite AMM with the objective of using frequency response characteristics to interpret the creation mechanisms of local resonance band gaps.

3. Transfer Functions and Pole-Zero Distributions

3.1. Transfer function of a 2-cell AMM

Starting with a 2-cell AMM of the same unit cell configuration (Figure 5(a)), we derive the transfer function relating the displacement of the second outer mass u_2 to an input force F applied to the first. The 2-cell AMM constitutes a 4 degree-of-freedom (DOF) system, with the DOFs being the outer and inner

mass displacements of the 2 cells. Following Eqs. (10) and (11), we can rewrite the motion equations in the Laplace domain via

$$U_1 = G(s)(k_a U_2 + k_b V_1 + F(s)) \quad (29)$$

$$U_2 = G(s)(k_a U_1 + k_b V_2) \quad (30)$$

$$\frac{V_2}{U_2} = \frac{V_1}{U_1} = H(s) \quad (31)$$

where the upper case $U_i(s)$ and $V_i(s)$ represent the displacements $u_i(t)$ and $v_i(t)$ in the Laplace domain, written as U_i and V_i for brevity, and the transfer functions $G(s)$ and $H(s)$ are given by $\frac{1}{m_a s^2 + (k_a + k_b)}$ and $\frac{k_b}{m_b s^2 + k_b}$, respectively. The dynamics of the 2-cell AMM can be graphically represented using the block diagram shown in Figure 5(b). The end-to-end transfer function U_2/F can be obtained from Eqs. (29) through (31) or by reducing the shown block diagram. We will use the block diagram reduction approach as it reveals some trends and consistent patterns in the dynamics of this class of locally resonant metamaterials that will be later used to generalize this framework for an AMM with any number of cells n .

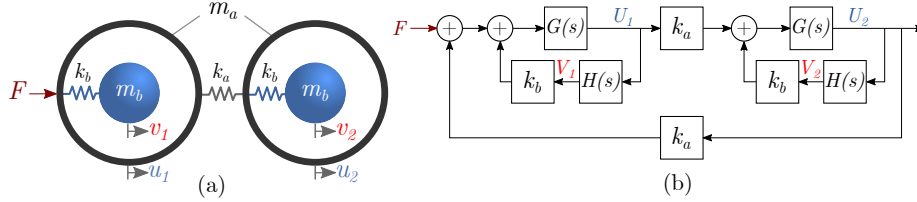


Figure 5: (a) Schematic and (b) Block diagram of a 2-cell locally resonant AMM

Moving the feedback gain k_a to the forward path, and making the necessary adjustments, reduces the system to the diagram in Figure 6(a), where the dashed boxes represent similar structures that can be replaced with the single transfer function T_1 as shown in Figure 6(b).

T_1 simplifies Eqs. (29) and (30) to the following form

$$U_1 = T_1(s)(U_2 + F(s)/k_a) \quad (32)$$

$$U_2 = T_1(s)U_1 \quad (33)$$

and is given by

$$T_1 = \frac{\alpha_1 s^2 + \alpha_2}{s^4 + \alpha_3 s^2 + \alpha_2} \quad (34)$$

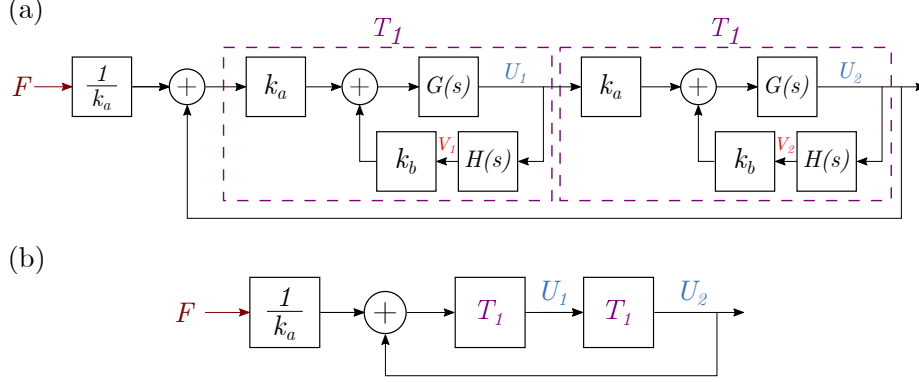


Figure 6: Block diagram of the 2-cell AMM reduced from Figure 5(b)

where $\alpha_1 = \omega_a^2 = \frac{k_a}{m_a}$, $\alpha_2 = \omega_a^2 \omega_b^2$, and $\alpha_3 = \omega_a^2 + \omega_b^2 + k_b/m_a$. Reducing Figure 6(b) to a single block gives the transfer function U_2/F

$$\frac{U_2}{F} = \frac{(\alpha_1 s^2 + \alpha_2)^2}{k_a s^2 (s^2 + (\alpha_3 - \alpha_1))(s^4 + (\alpha_3 + \alpha_1)s^2 + 2\alpha_2)} \quad (35)$$

The dynamics of the 2-cell AMM captured by Eq. (35) is graphically represented in Figure 7, for the same values of m_a , m_b , k_a , and k_b used earlier to plot the dispersion curves in Figure 2. As depicted in the transfer function, the AMM has two repeated poles at $s = 0$ and at $s = \pm j\omega_b \sqrt{1 + m_r}$ (p_1 and p_3 in Figure 7). The poles at the origin are representative of the AMM's rigid body modes since the system considered is unconstrained (i.e. free-free). The poles at $\pm j\omega_b \sqrt{1 + m_r}$ indicate the presence of a resonant frequency of the 4-DOF AMM right at the upper bound of the band gap, as given earlier by Eq. (6). The significance of the remaining poles will later become clear when the general case of an AMM with a n number of cells is discussed. On the other hand, the 2-cell AMM has repeated zeros at $s = \pm j\omega_b$ which is the stand-alone natural frequency of the local resonator. In this case, the 2-cell AMM acts as a vibration absorber with a tuned anti-resonance at ω_b where the response zeros out as shown by the frequency response in Figure 7(a). The formation of a band gap that spans a frequency range rather than a single frequency is not evident at this point.

3.2. General formulation for an n -cell AMM

Using a similar approach, and by utilizing the repeating patterns in the block structure of the AMM, a closed-form expression for the transfer function of a general lumped AMM with any given number of cells n can be derived. The obtained transfer function can specifically describe the displacement of any i^{th} cell in the AMM to a given forcing input. In the next steps, the exciting force F is still applied to the outer mass of the first AMM cell. Owing to the periodic nature of the AMM, the block diagram of n cells is now presented by a series

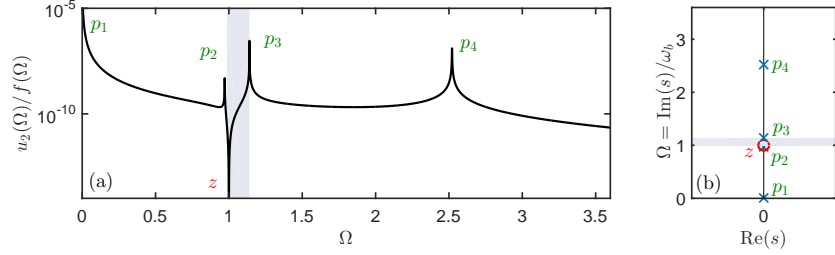


Figure 7: (a) Frequency response of the outer displacement of the second cell u_2 in a 2-cell AMM as a ratio of the input force f . (b) Corresponding pole-zero map of the U_2/F transfer function shown in Eq. (35). p and z denote the locations of the poles and zeros, respectively. The shaded region in both plots represents the band gap span of an infinite AMM as predicted by the unit cell dispersion relations in Figure 2

of nested unity feedback loops with two forward path transfer functions T_1 and T_2 , as shown in Figure 8. T_2 is given by

$$T_2 = \frac{\alpha_1 s^2 + \alpha_2}{s^4 + (\alpha_1 + \alpha_3)s^2 + 2\alpha_2} \quad (36)$$

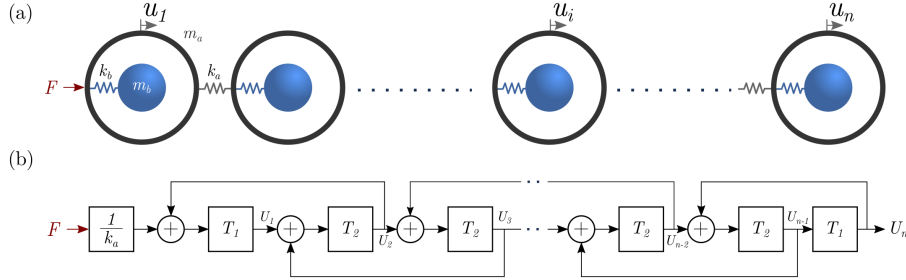


Figure 8: (a) Schematic of a finite realization of AMM with n number of cells and (b) its corresponding block diagram

One way to obtain an expression for the end-to-end transfer function U_n/F is to move the feedback branch from U_n to the left of last T_1 block. A reduced feedback loop B_{n-1} , highlighted in Figure 9, can be generated as a result. Note that the last block in Figure 9 is $B_n = T_1$. Moving backward and repeating this procedure yields another reduced block B_{n-2} that is a function of B_{n-1} , and so on. This process can be repeated n times going back all the way to the force input.

This repetitive process of computing the equivalent transfer function of the closed loop is found to be analogous to the continuous fraction technique [40], which can be used to obtain a general formula for the block $B_{n-(j+1)}$, as shown in Figure 10. The final form is shown in Figure 11.

$$B_n = B_3 = T_1 \quad (39)$$

$$j = 0 \neq (n-2) \quad B_{n-(j+1)} = B_2 = \frac{1}{\frac{1}{T_2} - T_1} = \frac{T_2}{1 - T_1 T_2} \quad (40)$$

$$j = 1 = (n-2) \quad B_{n-(j+1)} = B_1 = \frac{1}{\frac{1}{T_1} - \frac{1}{\frac{1}{T_2} - T_1}} = \frac{T_1(1 - T_1 T_2)}{1 - 2T_1 T_2} \quad (41)$$

which gives us the transfer functions:

$$\frac{U_3}{F} = \frac{1}{k_a} B_1 B_2 B_3 = \frac{1}{k_a} \frac{T_1^2 T_2}{1 - 2T_1 T_2} \quad (42)$$

$$\frac{U_2}{F} = \frac{1}{k_a} B_1 B_2 = \frac{1}{k_a} \frac{T_1 T_2}{1 - 2T_1 T_2} \quad (43)$$

$$\frac{U_1}{F} = \frac{1}{k_a} B_1 = \frac{1}{k_a} \frac{T_1(1 - T_1 T_2)}{1 - 2T_1 T_2}. \quad (44)$$

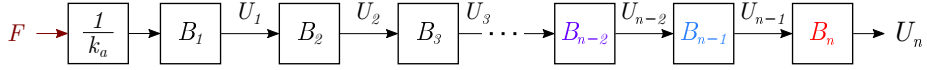


Figure 11: Block diagram of an n -cell AMM reduced from Figure 10

Consequently, and as can be inferred from Figure 11, the transfer function relating the displacement of the i^{th} cell to the force F applied at the first cell can be computed using the following sequence product

$$\frac{U_i}{F} = \frac{1}{k_a} \prod_{j=0}^{i-1} B_{j+1} \quad (45)$$

3.3. Limiting Case: Transfer function of an infinite AMM

An alternative form of Eq. (37), can be written as:

$$B_{n-(j+1)} = \frac{T_{2-\delta_{j,(n-2)}}}{1 - T_{2-\delta_{j,(n-2)}} B_{n-j}} \quad (46)$$

As the number of cells infinitely increases (i.e. $n \rightarrow \infty$), $B_{n-(j+1)}$ converges and becomes equal to its preceding value B_{n-j} . The converged $B_{n-(j+1)}$ and B_{n-j} functions will be denoted as Λ to distinguish them from the transfer function between two adjacent cells in a finite AMM. For an infinite chain of cells, $\delta_{j,(n-2)}$ will always be zero since all the cells can effectively be regarded

as inner cells in the infinite chain. As a result, Eq. (46) becomes a quadratic function which can be expressed as

$$T_2\Lambda^2 - \Lambda + T_2 = 0 \quad (47)$$

which leads to two solutions of Λ

$$\Lambda_{1,2} = \frac{1}{2T_2} \pm \sqrt{\frac{1}{4T_2^2} - 1} \quad (48)$$

Since Λ represents the transfer function between two neighboring cells, it can serve as the eigenvalues of the periodic transfer matrix and hence can be written as

$$\Lambda = e^{\bar{\beta}} = e^{\alpha+i\beta} \quad (49)$$

where α is the attenuation constant and β defines the phase difference between the adjacent cells [41]. Consequently, the variation of α and β with frequency can be determined for an infinite AMM, as shown in Figure 12. These variations perfectly coincide with the dispersion characteristics given earlier by the band structure in Figure 2 and calculated from Eqs. (48) and (49), thereby confirming the limiting case of the continuous fraction transfer function model.

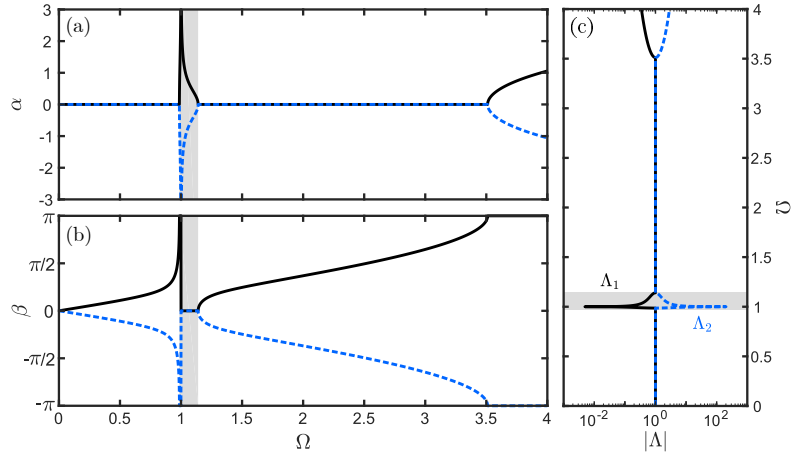


Figure 12: The frequency response of (a) the attenuation constant α , (b) the phase difference β and (c) the absolute value of the transfer function $|\Lambda|$ for an AMM with the same parameters used to generate Figure 2. Any value other than unity for $|\Lambda|$ indicates a band gap (shaded areas)

3.4. Frequency Response Functions

The different frequency response functions (FRFs) of the AMM can be obtained by substituting $s = j\omega$, where ω is the driving frequency, and writing

T_1 and T_2 in the frequency domain. Dividing throughout by ω_b^4 and with a few manipulations, we obtain

$$T_1(\Omega) = \frac{\Gamma(1 - \Omega^2)}{\Omega^4 - (\Gamma + m_r + 1)\Omega^2 + \Gamma} \quad (50)$$

and

$$T_2(\Omega) = \frac{\Gamma(1 - \Omega^2)}{\Omega^4 - (2\Gamma + m_r + 1)\Omega^2 + 2\Gamma} \quad (51)$$

The frequency response function $U_i(\Omega)/F(\Omega)$ can be found from Eq. (45) using $T_1(\Omega)$ and $T_2(\Omega)$, and thus can be expressed as

$$\frac{U_i}{F} = \frac{Z_i(\Omega)}{P(\Omega)} = \frac{1}{k_a} \sum_{q=1}^{2n} \frac{a_q}{\Omega^2 - \Omega_q^2} \quad (52)$$

where a_q is the residue of the q^{th} pole Ω_q while $Z_i(\Omega)$ and $P(\Omega)$ are the zeros and the poles polynomials, respectively. The values of the poles Ω_q are found using Eq. (24). The zeros polynomial $Z_i(\Omega)$ can be found from the determinant of a submatrix of Eq. (21) that result from deleting the row and the column corresponding to the excitation and sensing locations, respectively [42]. This determinant represents the poles of two substructures of the system that are before and after the actuation and sensing locations, respectively, when the displacement of both locations is constrained. In our case, the forcing input is always at the outer mass of the first cell and the number of zeros sandwiched between poles will be $2(n-i)$, in addition to i repeated zeros due to the presence of the local resonators. Following the scheme presented in [42], it can be shown that

$$Z_i(\Omega) = \left| \begin{array}{c} \Gamma\Omega - \mathbf{I} \\ i \times i \end{array} \right| \left| \begin{array}{c} \Omega^2 - (\Gamma\bar{\Psi} + (m_r + 1)\mathbf{I})\Omega + \Gamma\bar{\Psi} \\ n-i \times n-i \end{array} \right| \quad (53)$$

where $\bar{\Psi} = \Psi(i+1 : n, i+1 : n)$ is a submatrix of Ψ . Using the same methodology described in Eqs. (18) through (27) to analytically obtain the natural frequencies, $|\Omega^2 - (\Gamma\bar{\Psi} + (m_r + 1)\mathbf{I})\Omega + \Gamma\bar{\Psi}|$ can be found. As a result, $Z_i(\Omega)$ can be obtained as

$$Z_i(\Omega) = \Gamma^i (\Omega^2 - 1)^i \prod_{k=1}^{n-i} \Omega_k^4 - (1 + m_r + 2\Gamma(1 - \cos\theta_k))\Omega_k^2 + 2\Gamma(1 - \cos\theta_k) \quad (54)$$

where θ_k in this case is equal to $\frac{2k-1}{2(n-i)+1}\pi$ [39]. Multiplying both sides of Eq. (52) by $\Omega^2 - \Omega_q^2$ and evaluating the whole equation at $\Omega = \Omega_q$, the partial fraction coefficients are found to be

$$a_q = \frac{Z_i(\Omega_q)}{k_a \prod_{\substack{p=1 \\ p \neq q}}^{2n} \Omega_q^2 - \Omega_p^2} \quad (55)$$

For the end-to-end transfer function U_n/F , the sensing location i is equal to n and $Z_n(\Omega)$ is simply calculated via the determinant of $[\Gamma\Omega - \mathbf{I}]_{n \times n}$, hence

$$\frac{U_n}{F} = \frac{Z_n(\Omega)}{P(\Omega)} = \frac{\Gamma^n(\Omega^2 - 1)^n}{k_a \prod_{q=1}^{2n} \Omega^2 - \Omega_q^2} \quad (56)$$

and the partial fraction coefficients are then given by

$$a_q = \frac{\Gamma^n(\Omega_q^2 - 1)^n}{k_a \prod_{\substack{p=1 \\ p \neq q}}^{2n} \Omega_q^2 - \Omega_p^2} \quad (57)$$

Comparing Eqs. (56) and (52), a couple of observations can be made: 1) the term $(\Omega^2 - 1)$ in both numerators yields the repeated zeros at $\Omega = 1$. Since $i < n$, the number of these repeated zeros for the U_i/F transfer function are less than its U_n/F counterpart. 2) The repeated zeros at $\Omega = 1$ are the only numerator roots for U_n/F , while a number of anti-resonances are sandwiched in between the resonant frequencies as evident by the last term of $Z_i(\Omega)$ in Eq. (54). These differences exemplify the effect of changing the sensor location on the system's transfer function, i.e., the location of the cell of which the displacement is measured along the length of the AMM. Both observations will be depicted clearly in the numerical example presented next.

Finally, Figure 13 shows the residues of the end-to-end transfer function from Eq. (57) of an AMM of 100 unit cells. The values of the residues provide the contribution of each natural frequency to the AMM's response if the system is excited with an impulse force. It is clear that the values of the residues decrease significantly for the poles in the vicinity of the band gap (shaded region), indicating that these poles have the least contribution.

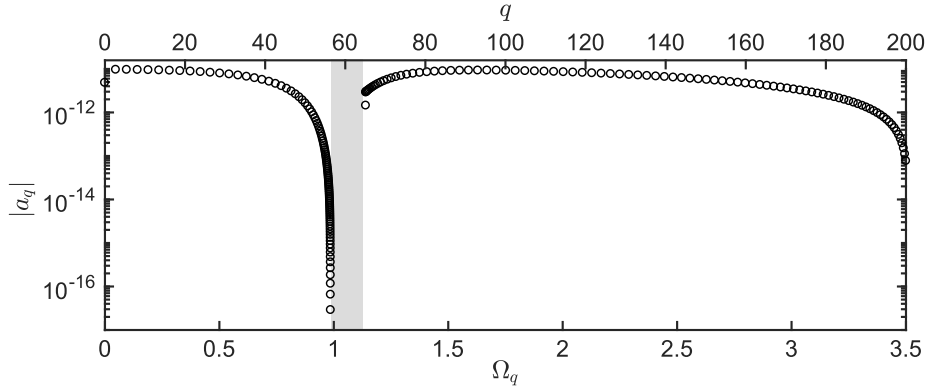


Figure 13: Residues of the end-to-end transfer function (Eq. (57)) for an AMM of $n = 100$

4. Numerical Validation

4.1. Increasing the number of cells

We start by considering the AMM shown in Figure 8(a) with four different number of cells: $n = 5, 10, 20$ and 50 . The value of the four cell parameters $m_a, m_b, k_a,$ and k_b are kept the same as those used earlier. Throughout this section, the focus is on the behavior of the last cell in the AMM chain in response to a force applied at the very first cell. For a sinusoidal force with a 1 N amplitude sweeping the frequency range $0 < \Omega < 3.5$, the frequency response of the displacements of the inner and outer masses of the last cell along with the corresponding pole-zero maps are displayed in Figure 14.

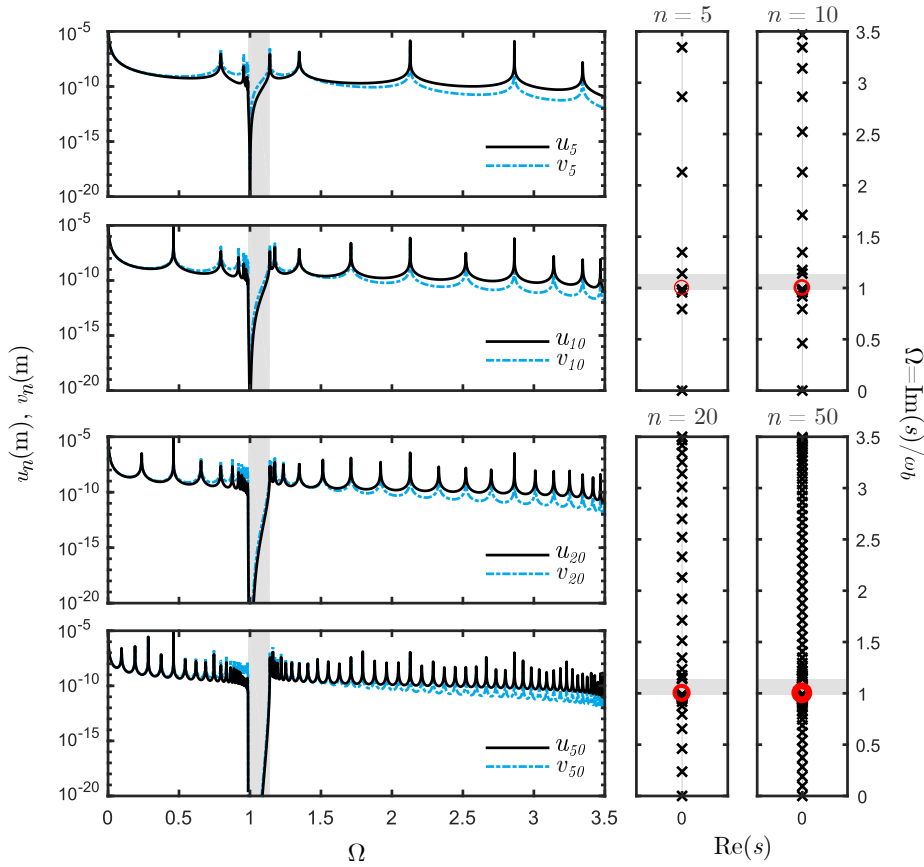


Figure 14: Frequency response of the outer and inner masses of the last cell, u_n and v_n , to an external force applied to the first cell for an AMM with $n = 5, 10, 20,$ and 50 cells (left column) and the corresponding pole-zero maps on the right columns. Poles and zeros are marked with crosses and circles, respectively. A thicker zero marker indicates larger algebraic multiplicity at $\Omega = 1$

The FRFs can be directly obtained from the harmonic analysis described in Eq. (12) or, equivalently, from the transfer function derived in Eq. (56). At a

first glance, the plots show that as the number of cells of the AMM increases, the width of the zeroed out (below 10^{-20}) part of the response gradually increases and eventually spans the theoretically predicted band gap range of an infinite AMM, represented by the shaded region in Figure 14. In other words, the AMM departs from a structure that absorbs an incident excitation at a single tuned frequency (as shown earlier in Figure 7) to one that almost perfectly attenuates incident waves over a continuous frequency range, a behavior which best describes the commonly known metamaterial band gap.

The mechanism by which the emergence of a band gap behavior happens in a finite locally resonant structure with increasing the number of cells can be understood in light of the transfer functions derived in Section 3. The formation of the band gap is the result of three distinct phenomena that take place simultaneously in the dynamics of the AMM system. We will go over each of them separately in the next section.

4.2. The formation mechanism of the band gap

4.2.1. The multiplicity effect of the locally resonant zero

As predicted by the derived transfer function in Eq. (56), increasing the number of cells of the AMM does not add zeros at new locations but rather increases the number of the repeated zeros at $\Omega = 1$. While obvious from the numerator of the derived function, the fact that a locally resonant AMM with any number of cells n has only one distinct zero location can be lost if the analysis is solely based on a numerical simulation. Figure 15 shows a common discrepancy obtained when using MATLAB's *pzmap* operator to obtain the distribution of zeros for this same example.

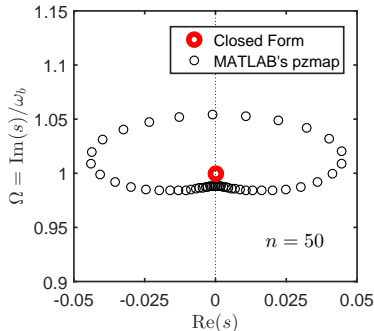


Figure 15: Zeros of the transfer function U_n/F of an AMM with $n = 50$ as calculated using the closed-form expression in Eq. (56) and numerically using MATLAB's *pzmap* operator

The figure, incorrectly, shows several zeros both above and below $\Omega = 1$ with non-zero real components. Since the AMM under consideration is non-dissipative and lacks any damping elements, the roots of both the numerator and the denominator of the closed-form transfer function have to be purely imaginary (i.e. lie on the imaginary axis of the s -plane). The shown behavior is a result of

numerical inaccuracies in the algorithm used by MATLAB to compute zeros in a system with high zero-multiplicity, which results in a cluster of approximate zeros distributed on a circle with a radius that is proportional to the machine precision [43]. This further signifies the importance of independently deriving the closed-form expression for the AMM's transfer function using the presented block diagram approach to eventually draw accurate conclusions.

Since the AMM's transfer function has a distinct zero location at $\Omega = 1$, the response ought to be absolutely equal to zero at ω_b only. Increasing the number of repeated zeros or numerator roots (commonly known as the algebraic multiplicity) only tends to flatten out the branches of the FRF around the zero location. The degree by which the branches bend outwards increases with the increase of the multiplicity or, in this case, the number of cells. As the number of cells approaches infinity, the numerator $Z_n(\Omega)$ in Eq. (56) approaches zero for any frequency Ω as long as the value of $\Gamma|(\Omega^2 - 1)|$ remains less than 1. Hence, this multiplicity effect is theoretically bounded by the range

$$\sqrt{1 - \frac{1}{\Gamma}} < \Omega < \sqrt{1 + \frac{1}{\Gamma}} \quad (58)$$

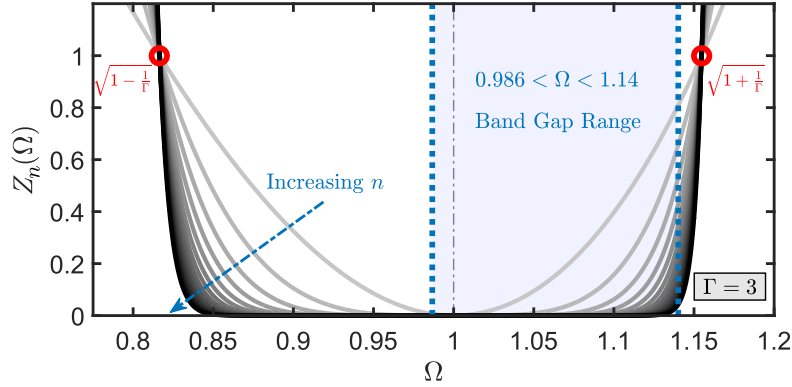


Figure 16: The effect of increasing the number of repeated roots (multiplicity) of the numerator polynomial $Z_n(\Omega)$ with the increase in the number of cells n in an AMM with $\Gamma = 3$

Figure 16 shows the variation of $Z_n(\Omega)$ with the number of cells n for $\Gamma = 3$. It can be seen that even though the AMM has a single zero location at $\Omega = 1$, increasing n gradually increases the frequency range over which Z_n approaches zero via the multiplicity effect, thus widening the potential region over which the vibrations can be largely attenuated. This concept of placing multiple zeros has been exploited for robust time-delay filter design for shaping reference inputs to minimize residual vibrations of lightly damped structures [44, 45]. This effect however, as predicted, is limited to the region bounded by Eq. (58) which, in this case, corresponds to $0.816 < \Omega < 1.154$. Also worth noting, is the fact that all curves in Figure 16 with different multiplicity orders intersect at $\Omega = \sqrt{1 - \frac{1}{\Gamma}}$

and $\Omega = \sqrt{1 + \frac{1}{\Gamma}}$, for values of Γ greater than 1. However, the lower bound on the multiplicity effect ceases to exist for $\Gamma < 1$, as shown in Figure 17.

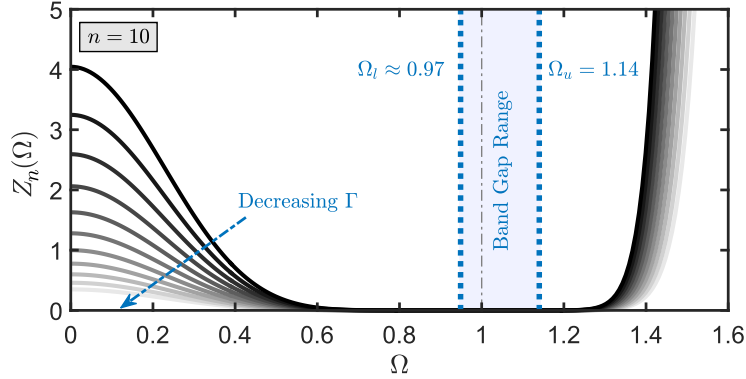


Figure 17: The effect of varying Γ on the numerator polynomial $Z_n(\Omega)$ for an AMM with a fixed number of cells ($n = 10$). The mass ratio in this simulation is kept constant and equal to 0.3. Different values of Γ result in changing the lower band gap, which, in this case, slightly varies around $\Omega_l = 0.97$

4.2.2. The enforced poles at the band gap bounds

The multiplicity range derived in Eq. (58) does not match the theoretical band gap bounds derived in Eqs. (5) and (6), and later observed in the FRFs of Figure 14(d) for a sufficiently large number of cells. In fact, Figures 16 and 17 suggest that the band gap can extend well beyond the theoretical limits if the analysis is solely based on the transfer function zeros. The second factor contributing to the formation of the band gap, as predicted theoretically, is the location of the transfer function poles in the vicinity of $\Omega = 1$. The roots of the characteristic polynomial $P(\Omega)$ of the transfer function U_n/F contains a set of repeated poles at $\Omega_u = \sqrt{1 + m_r}$, which is found by substituting $k = 1$ in Eq. (24). By knowing the value of the AMM masses, and hence m_r , the location of these poles can be determined and will be fixed irrespective of the number of cells n . The resonance peak at $\Omega_u = \sqrt{1 + m_r}$ can be, therefore, clearly seen in all four FRF plots of Figure 14. The location of these poles precisely coincides with Ω_u , the upper band gap bound of the infinite AMM. This means that as the multiplicity of zeros attempts to flatten out the frequency response curve around $\Omega = 1$, this effect is abruptly terminated at $\Omega_u = \sqrt{1 + m_r}$ due to the presence of a resonant frequency of the bulk structure. The FRF responds by moving quickly from a near-zero oscillation to a state of resonance and an extremely large amplitude. The same behavior takes place at the other end of the band gap thus constituting the formation of what appears to be a zeroed response over a continuous frequency range, or the band gap. The lower bound of the band gap, Ω_l , is also a pole that can be obtained from Eq. (24) by substituting $k = n$. Unlike Ω_u , this pole is not fixed and moves slowly with changing n . Although local resonance band gaps are commonly understood to

start at $\Omega = 1$, Ω_l is actually always going to be smaller than 1. In this example, for $n = 50$, Ω_l is calculated to be 0.9866 to the nearest 4th decimal place. Figure 18 shows the number of cells n needed for Ω_l to converge as a function of both mass and stiffness ratios, m_r and k_r , respectively. The convergence criteria is chosen such that the absolute difference between the value of the last pole in the acoustic mode (obtained from Eq. (24)) and Ω_l (obtained from Eq. (5)) is less than 1%. It is seen that with $m_r > 1$, the convergence tends to saturate at a specific value of k_r , but a larger number of cells is needed for a larger k_r at a given m_r value. For $m_r < 1$ and $0.01 < k_r < 100$, both k_r and m_r contribute equally to Ω_l convergence. The value of Ω_u remains invariant for all values of k_r and n as it is only a function of m_r . In other words, setting $k = 1$ always results in $\cos \theta_k = 1$ in Eq. (24) which yields the solution $\Omega_{1+n} = \Omega_u$.

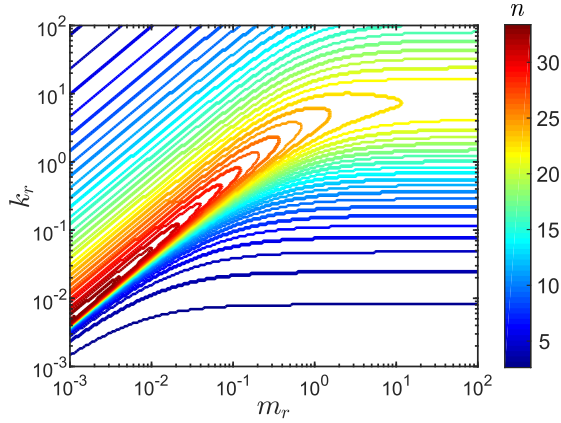


Figure 18: Convergence of Ω_l to its theoretical value as a function of both k_r and m_r .

4.2.3. The absence of poles in the band gap range

The last phenomenon that factors into the formation of the band gap in a finite AMM is the absence of resonances in the band gap frequency range. From Eq. (24), substituting the extreme values of $\cos \theta_k$ (i.e. 1 and -1) provides the largest/lowest values of natural frequencies that can be obtained. The two positive roots of the analytical formula for the natural frequencies are:

$$\Omega_{k_{\pm}} = \sqrt{\frac{1 + m_r + 2\Gamma(1 - \cos \theta_k)}{2} \pm \frac{\sqrt{(1 + m_r + 2\Gamma(1 - \cos \theta_k))^2 - 8\Gamma(1 - \cos \theta_k)}}{2}} \quad (59)$$

where Ω_{k_-} lies in the acoustic mode while Ω_{k_+} is in the optic mode. In case of $\cos \theta_k = 1$, $\Omega_{k_{\pm}} = 0, \sqrt{1 + m_r}$, which are the rigid body mode and the upper bound of the band gap, as indicated earlier. If $\cos \theta_k = -1$, the two solutions

are given by:

$$\Omega_{k_{\pm}} = \sqrt{\frac{1 + m_r + 4\Gamma}{2} \pm \frac{\sqrt{(1 + m_r + 4\Gamma)^2 - 16\Gamma}}{2}} \quad (60)$$

These two roots are the lower band gap limit $\Omega_{k_-} = \Omega_l$ and the limit at which the unbounded *stop band* starts [46]. This condition of $\cos \theta_k = -1$ is, however, not possible since it requires k (which has a maximum possible value of n) to be equal to $n + 1$. Hence, a finite AMM will have natural frequencies in the proximity of these two roots as the number of cells increases. Combining all cases shows that the possible natural frequencies are within two ranges:

$$0 \leq \Omega_{k_-} < \Omega_l \quad (61)$$

$$\Omega_u \leq \Omega_{k_+} < \sqrt{\frac{1 + m_r + 4\Gamma}{2} + \frac{\sqrt{(1 + m_r + 4\Gamma)^2 - 16\Gamma}}{2}} \quad (62)$$

which do not lie within the band gap region. Figure 19 graphically illustrates the regions where Eq. (24) crosses the zero-plane. As predicted, there are no solutions within the band gap region.

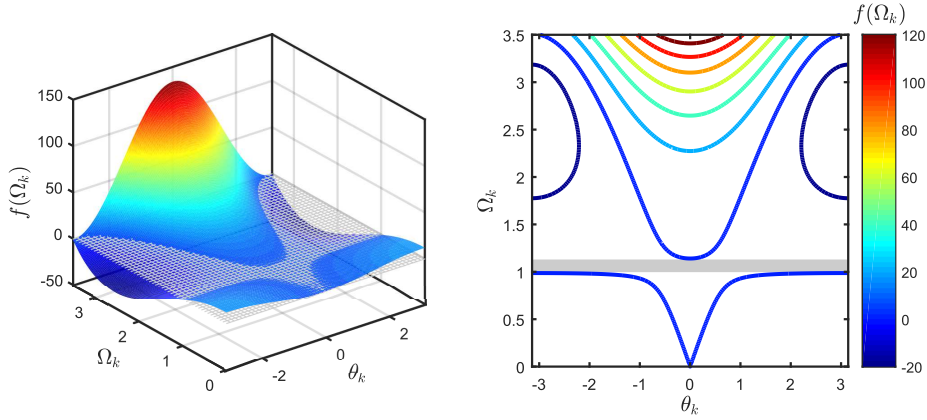


Figure 19: Evaluation of the system natural frequencies $f(\Omega_k)$ from Eq. (24) with variations of θ_k and Ω_k . The meshed plane in the left column shows intersection with the zero-plane at the roots of the equation

The pole-zero maps in Figure 14 interestingly show that, irrespective of the number of cells n that constitute the AMM, the overall system poles are equally split around the band gap range with no poles lying in the shaded region. In the previous section, it was explained how the presence of two resonance peaks flanking the repeated zeros at $\Omega = 1$, define the bandwidth of the band gap. This last phenomenon is, therefore, essential to ensure that the multiplicity effect which contributes to extending the effect of the single zero location over

the entire band gap range is not interrupted within the band gap. Finally, by adopting a linear scale and a close-up of the FRFs, Figure 20 nicely illustrates the evolution of the band gap from a single anti-resonance (for an AMM with $n = 2$) to a continuous attenuation over an extended range ($n = 50$).

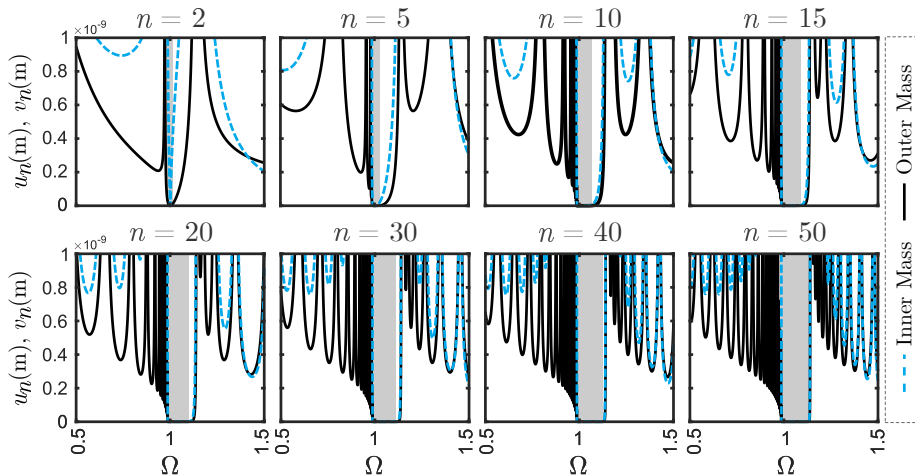


Figure 20: Evolution of the local resonance band gap in finite metamaterials from a 2-cell AMM upto a 50-cell AMM shown from left top corner to the right bottom corner. The shaded area shows the portion of FRF below 10^{-20} .

4.3. Effect of sensor location

In this section, we examine the spatial attenuation of the propagating wave from the excitation location at one end of the AMM to different locations along the length of the AMM. Hence, we shift our focus to the transfer function U_i/F derived in Eq. (52). For an AMM with $n = 10$ cells and the same values for the cell parameters m_a , m_b , k_a , and k_b , Figure 21 shows the frequency responses of the 1st, 4th, 7th and 10th (and last) cells, respectively, to an external force acting on the outer mass of the 1st cell and the corresponding pole-zero maps.

The FRFs shown in Figure 21 show that the degree of attenuation in the AMM increases as we move further away from the source, i.e., as i approaches n . From a transfer function perspective, the order of zero multiplicity (number of repeated zeros at $\Omega = 1$) is the same order as i , as captured by the $\Gamma^i(\Omega^2 - 1)^i$ term in the numerator $Z_i(\Omega)$ of Eq. (54). As the sensor is moved closer to the exciting force (i.e. as i approaches 1), some of these repeated zeros migrate to locations sandwiched between the system's poles. For a perfectly collocated sensor an actuator, each set of two neighboring poles will be separated by at least one zero. This zero migration behavior has been highlighted in literature in the context of controlled flexible structures [47, 48].

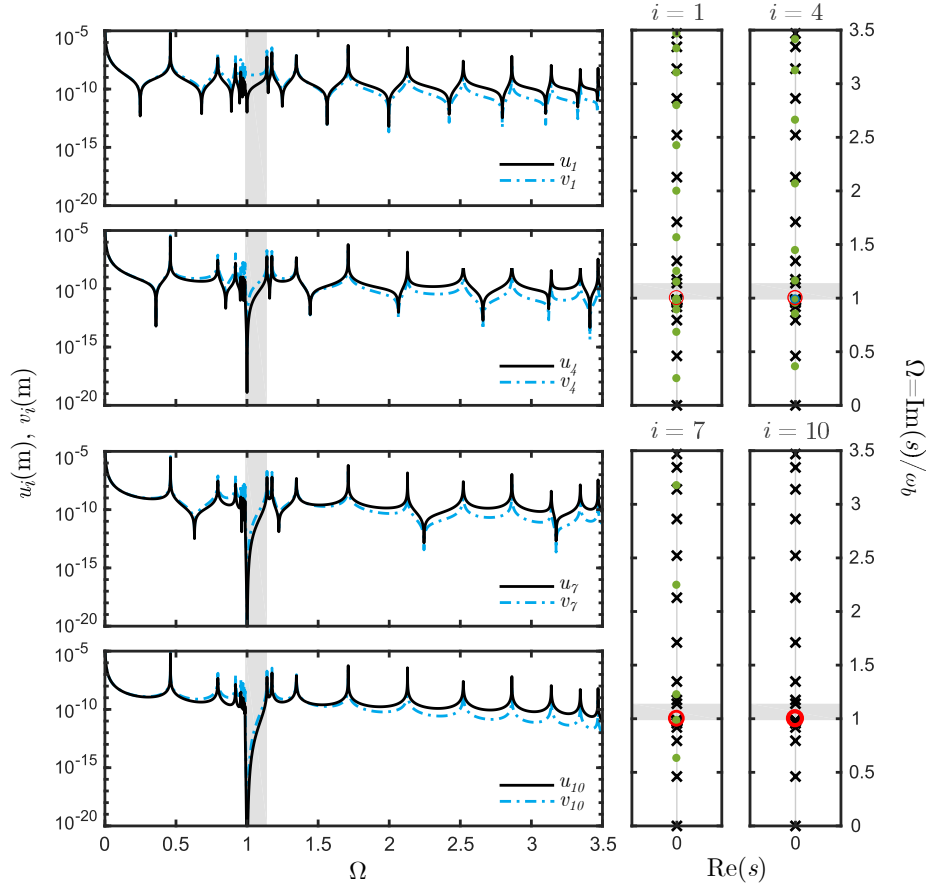


Figure 21: Frequency response of the outer and inner masses, u_i and v_i , of the 1st, 4th, 7th, and 10th (last) cell in an AMM with $n = 10$ cells (left column) along with their corresponding pole-zero maps (right columns). The red circles represents the zeros located at $\Omega = 1$, while the green dots are for the zeros caused from moving the measurement location. The poles are represented as black crosses.

5. Conclusions

This paper has presented an in-depth analysis of the formation of local resonance band gaps in locally resonant acoustic metamaterials of a finite length. A block diagram reduction approach was used to derive closed-form expressions for a lumped AMM with any number of cells n as well as at any cell location i . By deriving closed-form expressions for the force to end-displacement transfer functions, the frequency response of an AMM with a given set of parameters was obtained. The presented framework explained how the evolution of the band gap from a single anti-resonance to an attenuation of incident excitations over a continuous frequency range. The results are matched with the theoretical bounds of the band gap as derived by the commonly adopted Bloch-wave

model and the dispersion relations for a traveling wave in an infinitely-long metamaterial. The emergence of the local resonance band gap was explained using the derived system dynamics in light of three separate, yet simultaneous, phenomenon:

1. The existence of an n^{th} order multiplicity of repeated zeros at the distinct location of the local resonator ω_b which flattens out the FRF curves of the AMM's displacement, thus zeroing out the response around $\Omega = 1$.
2. The existence of system poles at both ends of the band gap that breaks the multiplicity effect. The pole north of the band gap is a fixed resonance at Ω_u that is independent of the number of cells and is solely a function of the mass ratio, while that south of the band gap varies with the AMM size and approaches its theoretical counterpart at sufficiently large values of n .
3. The distribution of poles on both sides of the band gap giving rise to different acoustic and optic resonant modes with the absence of any other poles in the band gap region.

The presented results facilitate the understanding of this type of local resonance band gaps in finite structures from a vibrations, rather than a wave-propagation standpoint. The study bridges the gap between the dispersion of waves in theoretical infinite structures and the structural dynamics of a finite, and thus physically realizable, locally resonant metamaterial. Finally, investigating AMMs in the context of frequency domain tools and PZ-maps sets a future framework for implementing robust control techniques.

References

- [1] Liu Z, Zhang X, Mao Y, Zhu Y, Yang Z, Chan CT, et al. Locally resonant sonic materials. *Science* 2000;289(5485):1734–6.
- [2] Huang HH, Sun CT. A study of band-gap phenomena of two locally resonant acoustic metamaterials. *Proceedings of the Institution of Mechanical Engineers, Part N: Journal of Nanoengineering and Nanosystems* 2011;;1740349911409981.
- [3] Huang GL, Sun CT. Band Gaps in a Multiresonator Acoustic Metamaterial. *Journal of Vibration and Acoustics* 2010;132(3):031003. doi:10.1115/1.4000784.
- [4] Wang G, Yu D, Wen J, Liu Y, Wen X. One-dimensional phononic crystals with locally resonant structures. *Physics Letters A* 2004;327(5):512–21.
- [5] Xiao Y, Wen J, Wen X. Longitudinal wave band gaps in metamaterial-based elastic rods containing multi-degree-of-freedom resonators. *New Journal of Physics* 2012;14(3):033042.

- [6] Yu D, Liu Y, Zhao H, Wang G, Qiu J. Flexural vibration band gaps in euler-bernoulli beams with locally resonant structures with two degrees of freedom. *Physical Review B* 2006;73(6):064301.
- [7] Yu D, Liu Y, Wang G, Zhao H, Qiu J. Flexural vibration band gaps in timoshenko beams with locally resonant structures. *Journal of Applied Physics* 2006;100(12):124901.
- [8] Sun H, Du X, Pai PF. Theory of metamaterial beams for broadband vibration absorption. *Journal of Intelligent Material Systems and Structures* 2010;.
- [9] Nouh M, Aldraihem O, Baz A. Vibration Characteristics of Metamaterial Beams With Periodic Local Resonances. *Journal of Vibration and Acoustics* 2014;136(6):61012. doi:10.1115/1.4028453.
- [10] Pai PF, Peng H, Jiang S. Acoustic metamaterial beams based on multi-frequency vibration absorbers. *International Journal of Mechanical Sciences* 2014;79:195–205.
- [11] Khajehtourian R, Hussein M. Dispersion characteristics of a nonlinear elastic metamaterial. *AIP Advances* 2014;4(12):124308.
- [12] Xiao Y, Wen J, Yu D, Wen X. Flexural wave propagation in beams with periodically attached vibration absorbers: band-gap behavior and band formation mechanisms. *Journal of Sound and Vibration* 2013;332(4):867–93.
- [13] Baravelli E, Ruzzene M. Internally resonating lattices for bandgap generation and low-frequency vibration control. *Journal of Sound and Vibration* 2013;332(25):6562–79. doi:10.1016/j.jsv.2013.08.014.
- [14] Zhu R, Liu X, Hu G, Sun C, Huang G. A chiral elastic metamaterial beam for broadband vibration suppression. *Journal of Sound and Vibration* 2014;333(10):2759–73. doi:10.1016/j.jsv.2014.01.009.
- [15] Krushynska A, Kouznetsova V, Geers M. Towards optimal design of locally resonant acoustic metamaterials. *Journal of the Mechanics and Physics of Solids* 2014;71:179–96.
- [16] Peng H, Pai PF. Acoustic metamaterial plates for elastic wave absorption and structural vibration suppression. *International Journal of Mechanical Sciences* 2014;89:350–61.
- [17] Wang Y, Wang Y. Complete bandgaps in two-dimensional phononic crystal slabs with resonators. *Journal of Applied Physics* 2013;114(4):043509.
- [18] Nouh M, Aldraihem O, Baz A. Wave propagation in metamaterial plates with periodic local resonances. *Journal of Sound and Vibration* 2015;341:53–73. doi:10.1016/j.jsv.2014.12.030.

- [19] Gonella S, To AC, Liu WK. Interplay between phononic bandgaps and piezoelectric microstructures for energy harvesting. *Journal of the Mechanics and Physics of Solids* 2009;57(3):621–33. doi:10.1016/j.jmps.2008.11.002.
- [20] Celli P, Gonella S. Tunable directivity in metamaterials with reconfigurable cell symmetry. *Applied Physics Letters* 2015;106(9). doi:10.1063/1.4914011.
- [21] Chen Y, Hu J, Huang G. A design of active elastic metamaterials for control of flexural waves using the transformation method. *Journal of Intelligent Material Systems and Structures* 2016;27(10):1337–47. doi:10.1177/1045389X15590273.
- [22] Chen Y, Huang G, Sun C. Band gap control in an active elastic metamaterial with negative capacitance piezoelectric shunting. *Journal of Vibration and Acoustics* 2014;136(6):061008.
- [23] Nouh M, Aldraihem O, Baz A. Periodic metamaterial plates with smart tunable local resonators. *Journal of Intelligent Material Systems and Structures* 2016;27(13):1829–45.
- [24] Bloch F. Über die quantenmechanik der elektronen in kristallgittern. *Zeitschrift für physik* 1929;52(7-8):555–600.
- [25] Hussein MI, Leamy MJ, Ruzzene M. Dynamics of Phononic Materials and Structures: Historical Origins, Recent Progress, and Future Outlook. *Applied Mechanics Reviews* 2014;66(4):040802. doi:10.1115/1.4026911.
- [26] Mead D. Free wave propagation in periodically supported, infinite beams. *Journal of Sound and Vibration* 1970;11(2):181–97. doi:10.1016/S0022-460X(70)80062-1.
- [27] Mead DJ. Vibration Response and Wave Propagation in Periodic Structures. *Journal of Engineering for Industry* 1971;93(3):783. doi:10.1115/1.3428014.
- [28] Faulkner MG, Hong DP. Free vibrations of a mono-coupled periodic system. *Journal of Sound and Vibration* 1985;99(1):29–42. doi:10.1016/0022-460X(85)90443-2.
- [29] Huang HH, Sun CT, Huang GL. On the negative effective mass density in acoustic metamaterials. *International Journal of Engineering Science* 2009;47(4):610–7.
- [30] Pai PF. Metamaterial-based Broadband Elastic Wave Absorber. *Journal of Intelligent Material Systems and Structures* 2010;21(5):517–28. doi:10.1177/1045389X09359436.

- [31] Gupta GS. Natural flexural waves and the normal modes of periodically-supported beams and plates. *Journal of Sound and Vibration* 1970;13(1):89–101.
- [32] Nielsen R, Sorokin S. Periodicity effects of axial waves in elastic compound rods. *Journal of Sound and Vibration* 2015;353:135–49.
- [33] Hvatov A, Sorokin S. Free vibrations of finite periodic structures in pass-and stop-bands of the counterpart infinite waveguides. *Journal of Sound and Vibration* 2015;347:200–17.
- [34] Sugino C, Leadenham S, Ruzzene M, Erturk A. On the mechanism of bandgap formation in locally resonant finite elastic metamaterials. *Journal of Applied Physics* 2016;120(13):134501.
- [35] Hussein MI, Frazier MJ. Metadamping: An emergent phenomenon in dissipative metamaterials. *Journal of Sound and Vibration* 2013;332(20):4767–74.
- [36] Frazier MJ, Hussein MI. Generalized bloch’s theorem for viscous metamaterials: Dispersion and effective properties based on frequencies and wavenumbers that are simultaneously complex. *Comptes Rendus Physique* 2016;17(5):565–77.
- [37] Chen Y, Barnhart M, Chen J, Hu G, Sun C, Huang G. Dissipative elastic metamaterials for broadband wave mitigation at subwavelength scale. *Composite Structures* 2016;136:358–71.
- [38] Andreassen E, Jensen JS. Analysis of phononic bandgap structures with dissipation. *Journal of Vibration and Acoustics* 2013;135(4):041015.
- [39] Yueh WC. Eigenvalues of several tridiagonal matrices. *Applied mathematics e-notes* 2005;5(66-74):210–30.
- [40] Hensley D. *Continued fractions; vol. 20.* World Scientific; 2006.
- [41] Al-Ba’ba’a H, Nouh M. An investigation of vibrational power flow in one-dimensional dissipative phononic structures. *Journal of Vibration and Acoustics* 2017;139(2):021003.
- [42] Miu D. *Mechatronics- Electromechanics and contromechanics (Book).* 1993.
- [43] Mathworks Documentation for MATLAB R2017a. <https://www.mathworks.com/help/control/ref/pole.html>; 2017.
- [44] Singh T, Vadali SR. Robust time delay control. *ASME Journal of Dynamic Systems, Measurement and Control* 1993;115(2(A)):303–6.
- [45] Singh T. *Optimal reference shaping for dynamical systems: theory and applications.* CRC Press; 2009.

- [46] Noh M. On the spatial sampling and beat effects in discrete wave profiles of lumped acoustic metamaterials. *The Journal of the Acoustical Society of America* 2017;141(3):1514–22.
- [47] Martin G. On the control of flexible mechanical systems. Ph.D. thesis; Stanford University; 1978.
- [48] Wie B, Bryson J. Modeling and control of flexible space structures. In: *Dynamics and control of large flexible aircrafts*. 1981, p. 153–74.